





Demonstration of mid-infrared slow light one-dimensional photonic crystal ring resonator with high-order photonic bandgap

FUJUN SUN,^{1,2,3,4} BOWEI DONG,^{2,3}  JINGXUAN WEI,^{2,3}  YIMING MA,^{2,3}  HUIPING TIAN,^{1,5} AND CHENGKUO LEE^{2,3,6} 

¹State Key Laboratory of Information Photonics and Optical Communications, Beijing University of Posts and Telecommunications, Beijing 100876, China

²Department of Electrical and Computer Engineering, National University of Singapore, 117583, Singapore

³Center for Intelligent Sensors and MEMS, National University of Singapore, 117608, Singapore

⁴Integrated Circuit Advanced Process Center, Institute of Microelectronics, Chinese Academy of Sciences, Beijing 100029, China

⁵hptian@bupt.edu.cn

⁶elelc@nus.edu.sg

Abstract: Integrated mid-infrared sensing offers opportunities for the compact, selective, label-free and non-invasive detection of the absorption fingerprints of many chemical compounds, which is of great scientific and technological importance. To achieve high sensitivity, the key is to boost the interaction between light and analytes. So far, approaches like leveraging the slow light effect, increasing optical path length and enhancing the electric field confinement (f) in the analyte are envisaged. Here, we experimentally investigate a slow light one-dimensional photonic crystal ring resonator operating at high-order photonic bandgap (PBG) in mid-infrared range, which features both strong field confinement in analyte and slow light effect. And the optical path length can also be improved by the resonator compared with waveguide structure. The characteristics of the first- and second-order bandgap edges are studied by changing the number of patterned periodical holes while keeping other parameters unchanged to confine the bands in the measurement range of our setup between 3.64 and 4.0 μm . Temperature sensitivity of different modes is also experimentally studied, which helps to understand the field confinement. Compared to the fundamental PBG edge modes, the second PBG edge modes show a higher field confinement in the analyte and a comparable group index, leading to larger light-matter interaction. Our work could be used for the design of ultra-sensitive integrated mid-infrared sensors, which have widespread applications including environment monitoring, biosensing and chemical analysis.

© 2020 Optical Society of America under the terms of the [OSA Open Access Publishing Agreement](#)

1. Introduction

Silicon photonics in the mid-infrared (MIR) region has been attracting more and more attention due to its potential for chemical and biological sensing by detecting the absorption spectrum at chip-level [1–5]. As known, the absorption spectroscopy sensing principle is based on the Beer-Lambert absorption method [5–8]. It describes the intensity of a light signal decaying through an absorption medium, $I = I_0 \exp(-\gamma\alpha L)$, where I_0 is the incident light intensity, α is the molar absorption coefficient, L is the optical path length, and γ is the absorption enhancement factor equal to 1 for free beam interaction. Since for Lab-on-chip systems, the physical length of the device must be small. While, slow light with remarkably low group velocity offers the possibility for the spatial compression of optical energy, which reduces the device footprint and enhances light-matter interactions, thus enhancing the absorption sensitivity [8–12]. Using the perturbation theory, previous study has demonstrated that the absorption enhancement factor γ

caused by the slow light can be expressed by $\gamma = f \times c / (n \cdot v_g)$, where c is the velocity of light in free space, v_g is the group velocity of input light in the device, n is the refractive index of the analyte and the fraction of optical field in the analyte f is defined as $f = \int_{air} \epsilon |E|^2 dV / \int_V \epsilon |E|^2 dV$ [12]. From this expression, we can deduce that to maximize the absorption sensitivity, the confinement factor f and the structural group index c/v_g should be as large as possible. Hence, a device supporting a mode that has slow light effect and a high electric field fraction f in the low refractive index region is necessary for the application of absorption spectroscopy, especially for the MIR molecular ‘fingerprint region’.

Slow light effect has been demonstrated in waveguide-based periodic structures in the MIR, including 2D photonic crystal (PhC) waveguide [13–14] and 1D grating waveguide [15]. Yet, for sensing applications, cavities exhibiting sharp resonance peaks are more attractive due to their strong field confinement ability in small regions to enhance light-matter interaction and to achieve a low detection limit. For example, different with waveguide structure, the optical path length for ring resonator is $L = Q \cdot \lambda / (2\pi n_{eff})$ [16], which is independence with the radius of the ring R . Therefore, the absorption sensitivity can also be enhanced by improving the Q -factor of the resonator to increase the interaction length. One of the cavity-based slow light enhanced structure is the photonic crystal ring (PhCR) resonator, which has been studied widely in the near-infrared wavelength range [17–21]. The PhCR resonator combines the whispering-gallery-mode (WGM) resonance of microring resonators with the slow-light effect presented in PhC waveguides. When the resonant modes are near the Brillouin zone edge, the free spectral range (FSR) is decreasing and nonuniform due to the increase of group index. Though one-dimension PhC nanobeam cavities can also achieve modes with slow light effect [22], compared with PhCR resonators it is hard to confine the modes at the bandgap edges to achieve high group index due to the tapered structural perturbation. While, the characteristics of PhCR resonator have never been studied in the MIR. Therefore, it is worth extending the operating range of PhCR resonators well into the MIR range.

In addition, multi-guided band gaps exist in a periodic dielectric waveguide, which means the slow-light enhanced effect can also be achieved at higher bandgap edges for PhCR structures, enabling the broadband operation in one structure. Moreover, higher-order band modes are more sensitive to environmental change due to the greater evanescent field fraction f located in the low refractive index region [23–24]. So they can also be used to enhance the absorption sensitivity according to the expression of absorption enhancement factor. Yet, previously only slow light characteristics at fundamental bandgap edges are studied. Therefore, here we demonstrate the feasibility and characteristics of the slow light effect at the second-order PBG edges of the PhCRs and compare with that at the first-order bandgap edges experimentally, which, to the best of our knowledge, has never been explored thoroughly. Limited by our experimental measurement wavelength range, we study the characteristics by fabricating PhCRs with different patterned periodical holes on normal rings. As a proof of concept, temperature sensing is demonstrated to illustrate that the second-order PBG mode has higher f than the first-order. Our work offers opportunities for the realization of MIR chemical and biological sensing with high absorption sensitivity, paving the way to integrated biomedical sensing and environmental monitoring systems.

2. Design and fabrication

Various silicon photonic material platforms, including silicon-on-insulator (SOI) [25–33], silicon-on-sapphire [7,10,34–35], silicon-on-nitride [36], as well as silicon-on-calcium-fluoride [5] have been demonstrated in MIR with low loss and favorable performance. Among these material platforms, SOI is undoubtedly the most popular one owing to its fabrication maturity and stability. Although the optical absorption loss caused by buried silicon dioxide (SiO₂) layer starts to

increase from $3.6\ \mu\text{m}$ onward, the SOI with SiO_2 layer can still be a promising candidate up to $6.0\ \mu\text{m}$ due to the high optical mode confinement in Si instead of SiO_2 [25–32].

Figure 1(a) shows the schematic structure of the proposed SOI PhCR device. The devices were fabricated by electron beam lithography (JEOL JBX-6300-100 kV) on SOI wafers with a $2\ \mu\text{m}$ buried oxide layer and a $500\ \text{nm}$ thick silicon (Si) layer. Electron beam lithography was performed using ZEP 520A resist spun at $6000\ \text{rpm}$ ($\sim 300\ \text{nm}$ thick). In order to save the writing time and cost, the beam current we choose is $5\ \text{nA}$, which has a beam diameter of $\sim 15\ \text{nm}$. An exposure dose of $300\ \mu\text{C}/\text{cm}^2$ was used. The resist is developed with n-Amyl acetate developer and rinsed with IPA/MIBK. The silicon layer is etched through to the buried oxide layer by reactive ion etching with C_4F_8 , SF_6 , and Ar process gases. Periodicity circular holes with radius r are embedded into the normal ring. For our devices, the radius of the PhCR R is $50\ \mu\text{m}$.

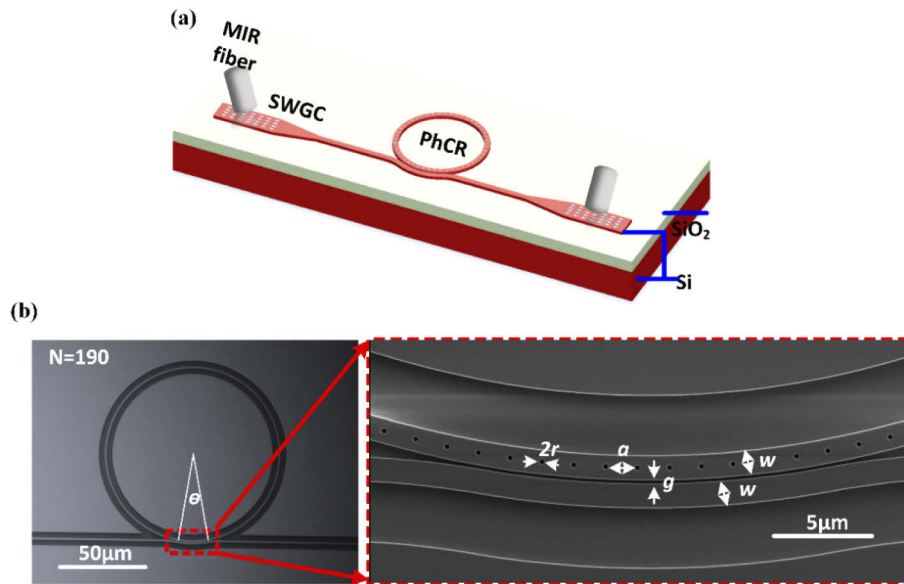


Fig. 1. (a) Schematic illustration of the SOI MIR PhCR in experiment, (b) Microscope image of the fabricated PhCR structure and the magnified SEM image of the coupling region.

The measurements were performed using a linearly polarized continuous wave tunable MIR laser ($3.64\text{--}4.12\ \mu\text{m}$) and detector. Details of the experimental set up were discussed in our previous works [32]. The light from the input fiber is coupled into the bus waveguide through a TE subwavelength grating coupler (SWGc), then passes through the PhCR, and finally gets directed out by the other grating coupler. (2). The periods of the SWGCs are chosen as $1.9\ \mu\text{m}$ and $1.0\ \mu\text{m}$ along and perpendicular to the waveguide propagation direction, and the corresponding trench widths are $1.026\ \mu\text{m}$ and $0.260\ \mu\text{m}$, respectively. The measured fiber–chip–fiber loss of the grating couplers on one side is $\sim 6\ \text{dB}$ at $3.750\ \mu\text{m}$ and the $3\ \text{dB}$ -bandwidth is about $\sim 170\ \text{nm}$. Figure 1(b) shows the top-view microscope image of a fabricated device. A close-up scanning electron micrograph (SEM) of the evanescent coupling region between PhCR and coupling waveguide is shown in the zoom-in picture. For the coupling region, the bus waveguide has a circular part around the PhCR over an angle of θ to ensure a good evanescent coupling between the bus waveguide and the PhCR resonator. The coupling region is approximately a uniform region with gap g . Compared with the conventional point coupling, the pulley coupling scheme here, which has an increased interaction length, makes the coupling quality factor (Q) and the extinction ratio depend on both the evanescent field overlap and phase matching. Therefore, a wider g range can be fabricated to get critical coupling. In the following experimental results,

the fabricated gap separation g is 120 nm. The width of the coupling bus waveguide and ring waveguide w both are set as 1.3 μm to minimize the absorption loss caused by SiO_2 and ensure the single mode condition. By changing the number of the patterned periodical circular air holes N , the corresponding lattice constant a ($a=2\pi R/N$) can be adjusted to make the bandgap edges fit into the required wavelength range. And the hole radius r can be chosen to tune the position of the edges exactly to some target wavelengths. Here, the characteristics of the first- and second-order bandgap edges in the wavelength range of 3.64~3.90 μm are studied by changing the number of patterned periodical holes N while other parameters remain unchanged. The theoretical analysis is described in the next section.

3. Band analysis

Because the bending losses of the PhCR can be neglected (the radius of the ring is large enough $R > \lambda/n_{\text{eff}}$), it is possible to approximate the PhCR by a straight waveguide with embedded periodic defects [17]. Therefore, the characteristics of the PhCR can be analyzed by calculating the dispersion of 1D PhC waveguide. Here, the dispersion curves are calculated using the Plane-Wave-Expansion (PWE) method with the super cell approach through the MIT Photonic Bands software package (MPB). Here, for calculations, we assumed the waveguide core refractive index of ~ 2.65 (equivalent to the effective refractive index of a 500 nm thick silicon slab for in-plane polarization at wavelength $\sim 3.75 \mu\text{m}$), the cladding refractive index of 1, the core width of 1.3 μm and the defect-hole diameter of 160 nm. When the number of the patterned periodical holes N is 380, the corresponding lattice constant a is $\sim 827 \text{ nm}$. The corresponding calculated TE band diagram is shown in Fig. 2(a). As can be seen, two band-gap regions PBG1 and PBG2 are formed due to the periodicity and the strong dielectric contrast. A larger first order bandgap PBG1 exists between the first dielectric band (1) and the first air band (2), which extends from roughly 3.633 μm to 3.767 μm , while an additional second-order bandgap PBG2 is established in the wavelength region from 2.751 μm to 2.822 μm . Bands (3) and (4) are referred to as the second dielectric band and the second air band respectively. Our characterization setup allows us to measure transmission spectra in the wavelength window ranging from 3.64 μm to 4.0 μm . Therefore, the number of the patterned periodical holes N is adjusted to make the photonic bandgap bound within this wavelength region while other parameters remain unchanged. Consequently, to observe PBG2 experimentally, N is fixed at 190, resulting in a period $\sim 1653 \text{ nm}$. The resultant PBG2 ranges from 3.733 μm to 3.781 μm of the device located in the measurement

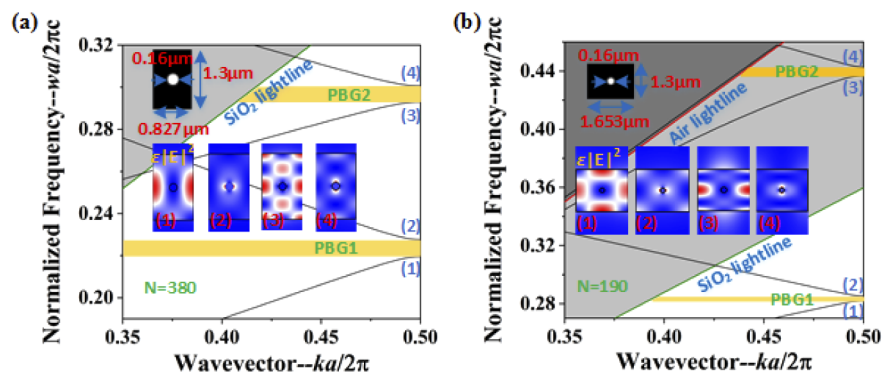


Fig. 2. Calculated dispersion diagram of the PhCR with (a) $N = 380$ and (b) $N = 190$. The first- and second-order photonic bandgaps PBG1 and PBG2 are indicated respectively and the inset shows the computed energy density distributions in one unit cell for the first four band edge modes.

range, while PBG1 ranged from 5.796 μm to 5.857 μm , as shown in Fig. 2(b). The corresponding energy density distributions for the first four bands for $N = 380$ and 190 presented in the mode diagram at the wave vector point $k=0.5$ in one unit cells are shown in the inset of Figs. 2(a) and (b). It is evident that unlike the dielectric bands whose energy is mostly confined in Si region, the energy of air bands is mostly confined inside the hole regions. And the calculated fractions of mode energy f inside the environmental medium for the 1, 2, 3 and 4 bands for $N = 380$ are 3.4%, 5.5%, 9.0% and 11.2% respectively, and for $N=190$ are 15.6%, 16.1%, 45.3% and 48.8%, respectively. From the calculated values, we can infer that compared with fundamental bandgap modes, higher-order bandgap modes will be more sensitive to environmental index changes. Another important observation here is that for $N = 380$, the PBG1 remains well below the light cone, while the PBG2 for $N = 190$ lies above the silica light line resulting in the relatively high f .

4. Results and discussion

To demonstrate the band gap characteristics of PBG1 and PBG2 calculated in Fig. 2, the normal ring and the PhCRs with patterned holes $N = 375, 380, 385, 185, 190$ and 195 (corresponding lattice constant are 0.838 μm , 0.827 μm , 0.816 μm , 1.698 μm , 1.653 μm and 1.611 μm , respectively) are fabricated and measured. The experimental transmission spectra are shown in Fig. 3. The measured spectra for PhCR resonators with different N are offset along the vertical axis for clarity. PhCRs with disturbed numbers ± 5 , relative to 380 and 190, are fabricated to study the wavelength tuning ability to make the position of resonance modes fit in some exact target wavelengths for different applications by changing the parameter of lattice constant. Though a mode is at the band edge only if the number of holes is even, the fundamental mode is still around the band edges when N is odd [37].

For normal ring resonators, as shown in Fig. 3(a), there are multiple resonator dips in the wavelength range of 3.64 to 3.90 μm with a uniform FSR ~ 16 nm and displays no PBG. Note that in order to achieve a high extinction ratio (ER) defined by the ratio between the on- and off-resonance transmission for the normal ring, an additional straight waveguide on the opposite side is also coupled to the normal ring resonator compared with the coupling structure in Fig. 1(b). The Q -factor and ER of the resonance at wavelength around 3.64748 μm are $\sim 11,292$ and 19 dB respectively obtained by the Lorentzian fitting, which is much higher than those around 3.89183 μm ($Q \sim 2,262$, ER ~ 8 dB). This can be attributed to the higher absorption loss of SiO_2 at wavelengths above 3.8 μm , which makes the critical coupling condition between bus waveguide and normal ring varying with the wavelength.

While, for all the PhCRs, PBGs are clearly exhibited as shown in Fig. 3(a). With the increase of N , the transmission spectra have a blue shift due to the decrease of the effective refractive index. Air and dielectric resonance modes are located on two sides of PBG regions, respectively. Due to the limited measurement laser range, we only achieve the transmission spectra of the air bands for $N=185, 190$ and 375. Close to the PBG edges, the resonance modes on two sides both exhibit non-uniform FSRs that rise with an increasing distance from the PBGs, indicating the presence of slow light. The non-uniformity can be attributed to the strong dispersion of photonic lattice near the PBG edges. As predicted, bandgaps PBG2 with a bandwidth of approximately 77 nm (from ~ 3.706 μm to 3.783 μm for $N = 190$) are clearly visible in the transmission spectra when the number of patterned holes N is around 190, agreeing with that of the bandgap calculations in both its width and position with good accuracy in Fig. 2(b). Similarly, for the transmission spectra with N of around 380, wider bandgaps PBG1 with a bandwidth of approximately 144 nm (from ~ 3.667 μm to 3.811 μm for $N = 375$) resulting from the larger contrast of the refractive index are also clearly observed. Additionally, the fluctuation of the number of the patterned hole 5 induced wavelength shift for $N = 380$ is weaker because the variation of lattice constant correspondingly changes from ~ 43 nm to ~ 10 nm for N changing from 190 to 380.

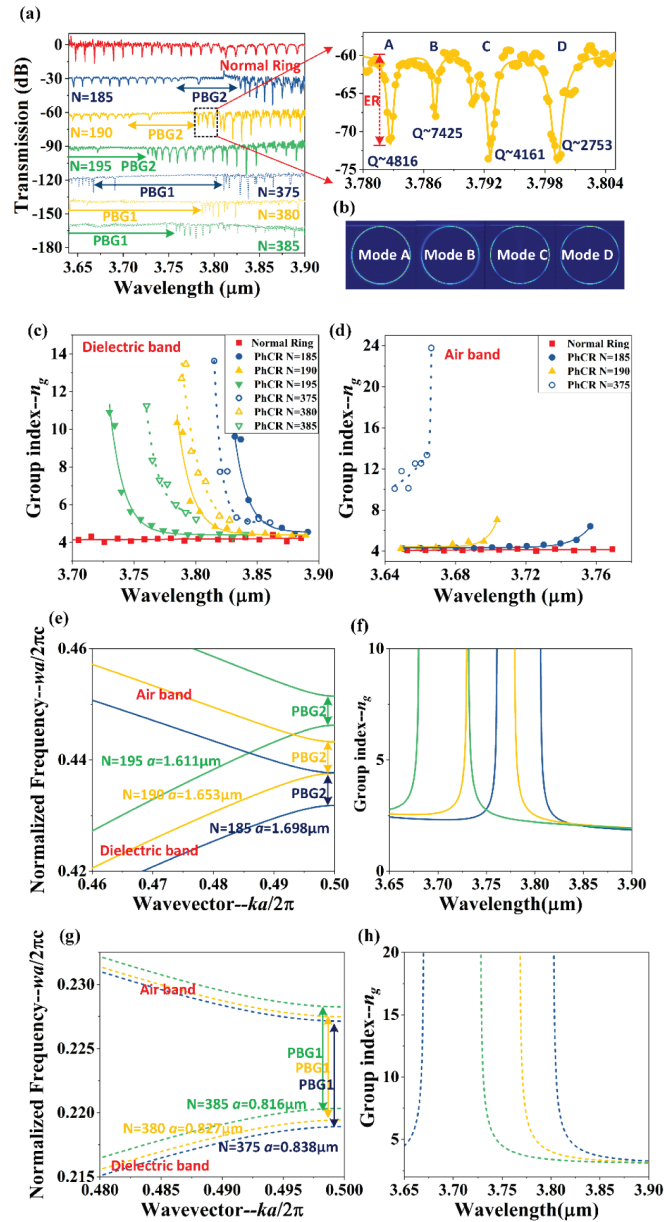


Fig. 3. (a) Measured transmission spectra of the normal ring and PhCRs with patterned numbers $N = 185, 190, 195, 375, 380$ and 385 respectively (corresponding lattice constant are $0.838 \mu\text{m}, 0.827 \mu\text{m}, 0.816 \mu\text{m}, 1.698 \mu\text{m}, 1.653 \mu\text{m}$ and $1.611 \mu\text{m}$, respectively). The inset shows the magnified dielectric modes closing the PBG with $N = 190$. The measured spectra for PhCR resonators with different N are offset along the vertical axis for clarity. (b) Simulated intensity profiles of modes A-D (c) Measured group index of the normal ring and PhCRs for the dielectric modes (d) Measured group index of the normal ring and PhCRs for the dielectric modes for the air modes (e) Simulated dispersion diagram of PhCRs with $N = 375, 380$ and 385 , and the corresponding calculated group index curves are shown in (f), (g) Simulated dispersion diagram of PhCRs with $N = 185, 190$ and 195 , and the corresponding calculated group index curves are shown in (h).

Taking $N = 190$ for example, the magnified transmission spectra of the four dielectric modes fitting with Lorentzian curves near the PBG2 edge are labeled as A, B, C, D and shown in the inset of Fig. 3(a). And their corresponding steady-state intensity profiles are shown in Fig. 3(b). As shown, for mode A, the electric field shows a uniform standing wave intensity, while all the other modes show an even number of nodes in the electric field resulting from the beating of two wave vectors. For mode A with a high ER ~ 12 dB at the wavelength of $3.783 \mu\text{m}$ nearest the band edge, the Q factor ($\sim 4,816$) is significantly higher than that ($\sim 3,004$) at the around resonance $3.785 \mu\text{m}$ for the normal ring. And the highest Q factor of 7,425 is obtained for mode B at the resonance $3.787 \mu\text{m}$ near the band edge. This is most likely because the Q -enhancement induced by dispersion overcomes the scattering loss due to the rough sidewalls of air holes. For mode C, there is a mode splitting, which may be caused by fabrication-induced surface roughness. Because the slightly different sizes of holes or reflections from the bus waveguide in the coupling region could break the frequency-degeneracy of modes. For $N = 380$, the Q -factor of the mode nearest the band edge at the wavelength of $\sim 3.787 \mu\text{m}$ is $\sim 6,107$ with ER ~ 11 dB. We can observe that even the higher-order bands exist in the radiation area, ER and Q are comparable to that of the first-order band modes. This is because higher-order bands originated from less patterned holes, indicating smaller fabrication induced scattering loss. This observation demonstrates that the fabrication induced dispersion loss affects the transmission characterizations seriously for this kind of side-coupled structure.

Figures 3(c) and (d) show the fitting of the calculated group index of the normal ring and PhCRs as a function of wavelength from the measured spectra in Fig. 3(a) by taking $n_g \approx \lambda^2 / \Delta\lambda L_R$, where n_g is the group index, λ is the central waveguide between two resonances, $\Delta\lambda$ is the FSR, and L_R is the round-trip path length of the ring. Figures 3(c) and (d) represent the measured group index of the dielectric and air modes at the PBG edges, respectively. As shown in Fig. 3(c), the change of lattice constant not only effects the position of the resonance wavelength, but also makes the bandwidth with higher group index increase with the increase of N while the highest group index almost keeps the same. To analyze the experimental results, the calculated group index using the dispersion curves simulated by MPB is performed. According to the slope of the dispersion-relation curve as shown in Figs. 3(e) and (g), we can obtain accurately the group index, which is calculated as $n_g = c/v_g = c \cdot dk/d\omega$. As shown in Figs. 3(f) and (h), the tendency of the calculated results are in agreement with the experimental results. When increasing N at fixed other parameters for a certain band, the band tends to become flatter and the group index at fixed wavelength increases. The small wavelength mismatch between the simulation and the experiments possibly is possibly caused by the fabrication imperfections or simulation parameter settings, such as effective refractive index and mesh accuracy. For N around 190, the averaged largest experimental group index of the dielectric bands is ~ 11 , corresponding to a slowdown factor of $S = n_g/n_p \approx 3.2$, where n_p is the phase index of silicon. The group index of the PhCR has an enhancement factor of 2.5 comparing to that of the normal ring ($n_g \approx 4$). While for N around 380, the averaged highest group index is ~ 14 , corresponding to a slowdown factor of $S \approx 4.1$ and an enhancement factor of 3.5 comparing to that of the normal ring. Therefore, using the calculated confinement factor and measured group index, for $N=190$ ($n_g=11, f=45.3\%$) and 380 ($n_g=14, f=3.4\%$), the corresponding absorption enhancement factors γ induced by slow light effect are ~ 5 and 0.5, respectively. In addition, for the cases of $N=190$ and 380 with $R=50\mu\text{m}$, the measured Q values are 4816 and 6107, respectively. Therefore, compared with the unfolded 1D photonic crystal waveguide structure ($L = 2\pi R$), the corresponding effective optical path length increases at least three-fold and four-fold, respectively. Therefore, our fabricated 1D PhCR resonators can achieve higher absorption sensitivity with a compact size compared with photonic crystal waveguide structures. To make a clear comparison about the performance of 1D PhCRs obtained in our paper, some related previously published papers have been presented in Table 1.

Table 1. λ_c , Q -factor, n_g , f and γ compared with different references

	Structure	λ_c	Q -factor	n_g	f	γ
The present work	1D PhCR with $N=190$	$\sim 3.783\mu\text{m}$	4816	~ 11	0.453	~ 5
	1D PhCR with $N=380$	$\sim 3.787\mu\text{m}$	6107	~ 13	0.034	~ 0.5
Ref. [18]	1D PhCR	$\sim 1545\text{nm}$	2500	17	–	–
Ref. [21]	1D PhCR	$\sim 1555\text{nm}$	1200	17	–	–
Ref. [10]	PhC waveguide	$\sim 3.43\mu\text{m}$	–	20	–	–
Ref. [11]	PhC waveguide	$\sim 1534\text{nm}$	–	6.7	–	0.31
Ref. [9]	Subwavelength grating waveguide	$\sim 1651\text{nm}$	–	5.6	0.2	1.1
Ref. [38]	Bloch slot waveguide	$\sim 3.31\mu\text{m}$	–	6.42	0.485	3.11

Figure 3(d) shows the measured group index for the air bands. Due to the radiation loss of the air modes are higher than the dielectric modes, the coupling between CWG and PhCR changed from critical for dielectric modes to under-coupled for air modes. Therefore, several modes near the band edges did not couple in, resulting in low measured group index for $N = 185$ and 190 here. For further studies, the width of the CWG can be optimized to achieve more effective coupling. Because the performance of the dielectric modes is better, so in the following sections we just focus on the dielectric modes in the vicinity of the band edge. In this section, we demonstrate that the modes at higher-order band edges can be observed with high ER and Q -factor, while the group index keeps similar to that in fundamental bands. And the period of the PhCR devices (number of patterned holes N) can be chosen to tune the position of the band edge exactly at the target wavelength.

To investigate the impact of holes radius r on the group index of the slow light modes near the band gap edges, PhCR devices for $N = 380$ and 190 with r varying from 80 nm to 160 nm with a step of 20 nm are fabricated and measured, while other parameters are fixed. The measured group index calculated from the transmission spectra for $N = 380$ and 190 are shown in Figs. 4(a) and (d), respectively. Clearly, with the increase of holes radius r , the modes move to shorter wavelengths as the effective index decreased locally. Moreover, the moving amount increases at larger r because of more band-edge field overlaps with the air area with the increase of r . In addition, as the radius r rises, the group index has a tendency to increase and the bandwidth in the slow light region is enlarged for both $N = 380$ and 190 . For $N = 380$, the largest group index for $r = 160\text{ nm}$ is ~ 23 , corresponding to an enhancement factor of ~ 5.7 comparing to that of normal ring. For $N = 190$, the group index for $r = 160\text{ nm}$ is ~ 25 , corresponding to an enhancement factor of ~ 6.3 . Certainly, with the increase of the air filling factor of the PhCRs, to achieve the phase matching condition, the width of the CWGs should be adjusted for further detailed studies. The corresponding dispersion curves simulated by MPB are also performed to verify the experimental results. As shown in Figs. 4(b) and (e), with the increase of r , the slope at large wavevectors decreases slowly in magnitude. Consequently, the calculated n_g curves increase slowly to an infinite value, and the increasing speed tends to be slower and slower with the increase of radius. Therefore, the wavelength range with a higher group index is wider and wider as shown in Figs. 4(c) and (f). This figure clearly illustrates the influence of radius r on the slow light properties for the first and second dielectric bands. These results suggest that the position and group index of the band edges modes can be engineered by tuning the radius of the patterned holes. Therefore, in practice, the radius of patterned holes can be designed to make the position of the band edge mode with the highest group index located in the region of the absorption peak of the analyte.

As known, for absorption sensing, the absorption factor determined by dispersion enhanced light-matter interaction can be expressed by $\gamma = f \cdot n_g/n$, indicating that the detection sensitivity

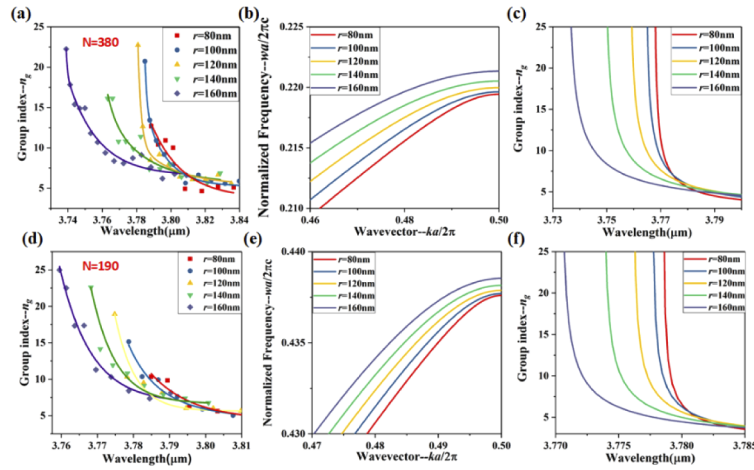


Fig. 4. (a) Measured group index curve variation, (b) dispersion band variation and (c) extracted group index variation with r , when $N = 380$; (d), (e) & (f) when $N = 190$.

can be enhanced by a larger group index and greater electric field confinement in the analyte. Therefore, here, an electric hot plate was attached to the bottom of the sample stage to control the temperature of the samples (PhCRs with $N = 380$ and 190 with $r = 80$ nm) simply to demonstrate the higher-order band dielectric mode has greater electric field overlap in the analyte due to the lower temperature sensitivity. The temperature sensitivity of silicon device theoretically is expressed as $S_T = f_{si} \cdot \frac{\lambda_c}{n_{si}} \cdot \frac{\partial n_{si}}{\partial T}$ [34], where f_{si} is the mode confinement in silicon region, λ_c is the resonance wavelength and $\frac{\partial n_{si}}{\partial T}$ is the thermo-optical coefficient of Si. For our fabricated PhCRs with $N=380$ and 190 , the wavelength of the resonance modes nearest the band gap edges are similar. And n_{si} and $\frac{\partial n_{si}}{\partial T}$ are only material dependent. Therefore, the difference between the temperature sensitivities is mainly caused by the mode confinement. On the other hand, by demonstrating the thermo-optic tuning ability of the PhCR device, we can make sure that the highest group index mode can be adjusted to locate in the region of absorption peak of the analyte in practical.

Figures 5(a) and (d) show the measured normalized transmission spectra at temperatures ranging from 25°C to 50°C and 25°C to 55°C respectively. Note that we put the fabricated chip on top of the sample stage, exposed to room environment. A simple adjustable temperature heating plate is attached to the bottom of the sample holder. Therefore, it needs a rather long time to heat up the stage steadily to higher than 55°C . As expected, as the temperature increased, the transmission peaks shift to longer wavelengths due to the increase of the core refractive index of the Si waveguide. Because the thermal-optical coefficient of Si is positive. The group indices of the PhCRs with increased temperature are deduced and fitted, as shown in Figs. 5(b) and (e). It is seen that the derived group index curve almost maintains its shape yet shifts to longer wavelengths with the increasing applied temperature, indicating the feasibility of thermo-optic tuning as well as the thermal stability of the average group index and the bandwidth. In the following study, a micro-heater can be integrated on the device for flexible dynamic tuning. For $N = 380$, when the device was heated up from 25°C to 50°C , the first resonance dip closest to the PBG1 shifts from $3.78814 \mu\text{m}$ to $3.7958 \mu\text{m}$, corresponding to a temperature sensitivity of $306 \text{ pm}/^\circ\text{C}$, as presented in Fig. 5(c). Note that the change of the Q -factor may be caused by the inhomogeneous heating induced unstable coupling condition. For $N = 190$, when the device was heated from 25°C to 55°C , the first resonance dip closest to the PBG2 shifts from $3.78327 \mu\text{m}$ to $3.79045 \mu\text{m}$, corresponding to a temperature sensitivity of $240 \text{ pm}/^\circ\text{C}$.

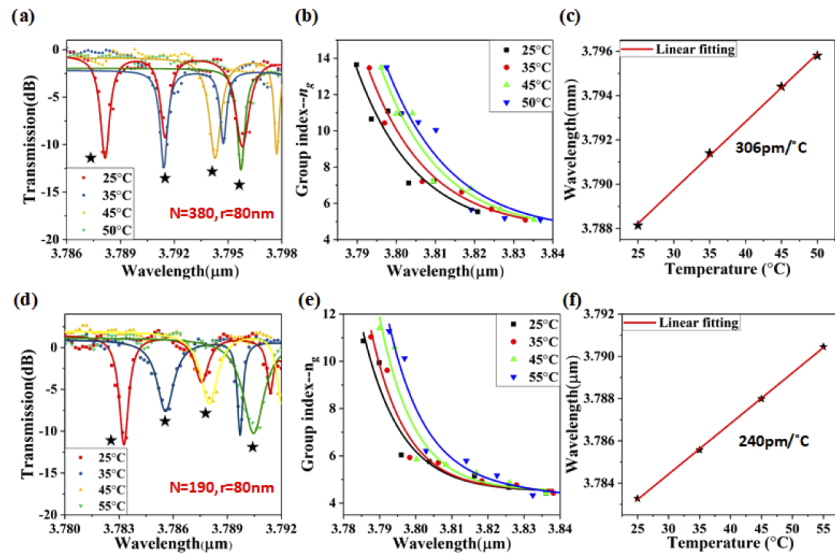


Fig. 5. (a) Measured transmission spectra variation, (b) extracted group index variation and (c) wavelength shift of the fundamental mode with temperature, when $N = 380$; (d), (e), (f) when $N = 190$.

Notably, both first- and second- bandgap edge modes exhibited good linearity over a wide range of temperatures. The PBG1 mode exhibited greater temperature-sensitivity than the PBG2 mode because stronger waveguide mode confinement existed in the PBG1 mode. Therefore, the result indicates that PBG2 mode has higher electric field fraction f in the low refractive index region, which is more suitable for absorption sensing. In addition, considering the calculated mode confinement factors in low refractive index region for them are 3.4% and 45.3%, respectively, the obtained experimental sensitivity difference between the PhCRs with $N=380$ and $N=190$ is not large enough as expected. The reasons may be the following two aspects. (1) The electric field fraction in the air region is calculated from the mode profile of the unit cell of 1D photonic crystal waveguide simulated using MPB. Therefore, there may have some computational errors. (2) The fabrication induced roughness (such as imperfect circular holes, rough sidewall and lag effect) may also be the reason for the discrepancy between the calculation and the experimental. For example, if the silicon layer isn't etched through to the SiO_2 layer for $N=190$, then the filed confinement factor in silicon will be higher in practice, resulting in higher temperature sensitivity. In the following studies, groups of devices should be fabricated and measured to get more detailed information. Here, we just provide a feasibility idea to study the characteristics of the fundamental and higher-order band gap modes.

5. Conclusion

In conclusion, we experimentally demonstrated and compared the slow light effect of the PhCRs in the first- and second-order PBG edges in MIR region. The influence of structural parameters (patterned holes N and radius r) on slow light properties was studied through theoretical analysis, simulation and experiment, providing a solid guideline on the design of PhCRs with strong slow light effect. For the second PBG edge modes with N around 190 and radius r 80 nm, the averaged largest group index of the dielectric bands of ~ 11 and highest Q factor of 7,425 are experimentally obtained. When r increases to 160 nm, the highest group index can be increased to ~ 25 , corresponding to an enhancement factor of ~ 6.3 . In addition, we performed the thermo-optic tuning by attaching a hot plate on the sample stage to demonstrate the second

bandgap edge modes have greater electric field overlap f in the analyte by comparing the temperature sensitivity. Therefore, with these two enhancement mechanisms n_g and f , the PBG2 modes are more suitable for absorption sensing based on $\gamma = f \cdot n_g/n$. Our results about the second PBG edge modes can be adopted in the realization of slow light effect for applications such as MIR absorption-based and NIR wavelength shift-based biochemical sensors with high sensitivity.

Funding

National Research Foundation Singapore (R-263-000-C24-281, R-263-000-C64-281); National University of Singapore (R-263-501-012-133); National Natural Science Foundation of China (61634006, 61372038, 61431003, 61904196); National Key Research and Development Program of China (2017YFA0205903, 2016YFB0402405); China Scholarship Council (201706470024).

Acknowledgments

Sun Fujun thanks the China Scholarship Council for supporting this work (File No. 201706470024).

Disclosures

The authors declare that there are no conflicts of interest related to this article.

References

1. R. Soref, "Mid-infrared photonics in silicon and germanium," *Nat. Photonics* **4**(8), 495–497 (2010).
2. T. Hu, B. Dong, X. Luo, T. Y. Liow, J. Song, C. Lee, and G. Q. Lo, "Silicon photonic platforms for mid-infrared applications," *Photonics Res.* **5**(5), 417–430 (2017).
3. Y. Zou, S. Chakravarty, C. J. Chung, X. Xu, and R. T. Chen, "Mid-infrared silicon photonic waveguides and devices," *Photonics Res.* **6**(4), 254–276 (2018).
4. V. Singh, P. T. Lin, N. Patel, H. Lin, L. Li, Y. Zou, F. Deng, C. Ni, J. Hu, J. Giammarco, A. P. Soliani, B. Zdyrko, I. Luzinov, S. Novak, J. Novak, P. Wachtel, S. Danto, J. D. Musgraves, K. Richardson, L. C. Kimerling, and A. M. Agarwal, "Mid-infrared materials and devices on a Si platform for optical sensing," *Sci. Technol. Adv. Mater.* **15**(1), 014603 (2014).
5. Y. Chen, H. Lin, J. Hu, and M. Li, "Heterogeneously integrated silicon photonics for the mid-infrared and spectroscopic sensing," *ACS Nano* **8**(7), 6955–6961 (2014).
6. Z. Han, P. Lin, V. Singh, L. Kimerling, J. Hu, K. Richardson, A. Agarwal, and D. T. H. Tan, "On-chip mid-infrared gas detection using chalcogenide glass waveguide," *Appl. Phys. Lett.* **108**(14), 141106 (2016).
7. N. Singh, A. Casas-Bedoya, D. D. Hudson, A. Read, E. Mägi, and B. J. Eggleton, "Mid-IR absorption sensing of heavy water using a silicon-on-sapphire waveguide," *Opt. Lett.* **41**(24), 5776–5779 (2016).
8. R. Jannesari, C. Ranacher, C. Consani, T. Grille, and B. Jakoby, "Sensitivity optimization of a photonic crystal ring resonator for gas sensing applications," *Sens. Actuators, A* **264**, 347–351 (2017).
9. A. Gervais, P. Jean, W. Shi, and S. LaRochelle, "Design of slow-light subwavelength grating waveguides for enhanced on-chip methane sensing by absorption spectroscopy," *IEEE J. Sel. Top. Quantum Electron.* **25**(3), 1–8 (2019).
10. Y. Zou, S. Chakravarty, P. Wray, and R. T. Chen, "Mid-infrared holey and slotted photonic crystal waveguides in silicon-on-sapphire for chemical warfare simulant detection," *Sens. Actuators, B* **221**, 1094–1103 (2015).
11. I. Dicaire, A. De Rossi, S. Combrié, and L. Thévenaz, "Probing molecular absorption under slow-light propagation using a photonic crystal waveguide," *Opt. Lett.* **37**(23), 4934–4936 (2012).
12. N. A. Mortensen and S. Xiao, "Slow-light enhancement of Beer-Lambert-Bouguer absorption," *Appl. Phys. Lett.* **90**(14), 141108 (2007).
13. C. Reimer, M. Nedeljkovic, D. J. M. Stothard, M. O. S. Esnault, C. Reardon, L. O'Faolain, M. Dunn, G. Z. Mashanovich, and T. F. Krauss, "Mid-infrared photonic crystal waveguides in silicon," *Opt. Express* **20**(28), 29361–29368 (2012).
14. Y. Ma, B. Dong, B. Li, K. W. Ang, and C. Lee, "Dispersion engineering and thermo-optic tuning in mid-infrared photonic crystal slow light waveguides on silicon-on-insulator," *Opt. Lett.* **43**(22), 5504–5507 (2018).
15. Y. Ma, B. Dong, B. Li, J. Wei, Y. Chang, C. P. Ho, and C. Lee, "Mid-infrared slow light engineering and tuning in 1-D grating waveguide," *IEEE J. Sel. Top. Quantum Electron.* **24**(6), 1–8 (2018).
16. Y. Sun and X. Fan, "Optical ring resonators for biochemical and chemical sensing," *Anal. Bioanal. Chem.* **399**(1), 205–211 (2011).
17. D. Goldring, U. Levy, and D. Mendlovic, "Highly dispersive micro-ring resonator based on one dimensional photonic crystal waveguide design and analysis," *Opt. Express* **15**(6), 3156–3168 (2007).

18. J. Y. Lee and P. M. Fauchet, "Slow-light dispersion in periodically patterned silicon microring resonators," *Opt. Lett.* **37**(1), 58–60 (2012).
19. K. McGarvey-Lechable, T. Hamidfar, D. Patel, L. Xu, D. V. Plant, and P. Bianucci, "Slow light in mass-produced, dispersion-engineered photonic crystal ring resonators," *Opt. Express* **25**(4), 3916–3926 (2017).
20. Y. Zhang, X. Qiu, C. Zeng, D. Li, G. Gao, Y. Wang, J. Yu, and J. Xia, "Slow-light dispersion in one-dimensional photonic crystal racetrack ring resonator," *IEEE Photonics Technol. Lett.* **27**(10), 1120–1123 (2015).
21. S. M. Lo, S. Hu, G. Gaur, Y. Kostoulas, S. M. Weiss, and P. M. Fauchet, "Photonic crystal microring resonator for label-free biosensing," *Opt. Express* **25**(6), 7046–7054 (2017).
22. F. Sun, J. Wei, B. Dong, Y. Ma, Y. Chang, H. Tian, and C. Lee, "Coexistence of air and dielectric modes in single nanocavity," *Opt. Express* **27**(10), 14085–14098 (2019).
23. S. Kim, H. M. Kim, and Y. H. Lee, "Single nanobeam optical sensor with a high Q-factor and high sensitivity," *Opt. Lett.* **40**(22), 5351–5354 (2015).
24. S. Surdo, F. Carpignano, S. Merlo, and G. Barillaro, "Near-Infrared Silicon Photonic Crystals with High-Order Photonic Bandgaps for High-Sensitivity Chemical Analysis of Water–Ethanol Mixtures," *ACS Sens.* **3**(11), 2223–2231 (2018).
25. M. M. Milošević, M. Nedeljkovic, T. M. Ben Masaud, E. Jaberansary, H. M. H. Chong, N. G. Emerson, G. T. Reed, and G. Z. Mashanovich, "Silicon waveguides and devices for the mid-infrared," *Appl. Phys. Lett.* **101**(12), 121105 (2012).
26. B. Dong, X. Guo, C. P. Ho, B. Li, H. Wang, C. Lee, X. Luo, and G. Q. Lo, "Silicon-on-insulator waveguide devices for broadband mid-infrared photonics," *IEEE Photonics J.* **9**(3), 1–10 (2017).
27. J. Wei, F. Sun, B. Dong, Y. Ma, Y. Chang, H. Tian, and C. Lee, "Deterministic aperiodic photonic crystal nanobeam supporting adjustable multiple mode-matched resonances," *Opt. Lett.* **43**(21), 5407–5410 (2018).
28. S. A. Miller, M. Yu, X. Ji, A. G. Griffith, J. Cardenas, A. L. Gaeta, and M. Lipson, "Low-loss silicon platform for broadband mid-infrared photonics," *Optica* **4**(7), 707–712 (2017).
29. Y. Chang, D. Hasan, B. Dong, J. Wei, Y. Ma, G. Zhou, and C. Lee, "All-dielectric surface-enhanced infrared absorption-based gas sensor using guided resonance," *ACS Appl. Mater. Interfaces* **10**(44), 38272–38279 (2018).
30. Y. Chang, B. Dong, Y. Ma, J. Wei, Z. Ren, and C. Lee, "Vernier effect-based tunable mid-infrared sensor using silicon-on-insulator cascaded rings," *Opt. Express* **28**(5), 6251–6260 (2020).
31. M. S. Yazici, D. Hasan, B. Dong, F. Sun, and C. Lee, "Integration of Thermopile on a Mid IR Waveguide," In *2019 International Conference on Optical MEMS and Nanophotonics (OMN)* (pp. 108–109). IEEE. (2019, July)
32. N. Chen, B. Dong, X. Luo, H. Wang, N. Singh, G. Lo, and C. Lee, "Efficient and broadband subwavelength grating coupler for 3.7 μm mid-infrared silicon photonics integration," *Opt. Express* **26**(20), 26242–26256 (2018).
33. Z. Cheng, X. Chen, C. Wong, Y. Chi, K. Xu, and H. Tsang, "Mid-infrared Suspended Membrane Waveguide and Ring Resonator on Silicon-on-Insulator," *IEEE Photonics J.* **4**(5), 1510–1519 (2012).
34. C. Wong, Z. Cheng, X. Chen, K. Xu, and H. Tsang, "Characterization of Mid-Infrared Silicon-on-Sapphire Microring Resonators With Thermal Tuning," *IEEE Photonics J.* **4**(4), 1095–1102 (2012).
35. T. Baehr-Jones, A. Spott, R. Ilic, A. Spott, and M. Hochberg, "Silicon-on-sapphire integrated waveguides for the mid-infrared," *Opt. Express* **18**(12), 12127–12135 (2010).
36. S. Khan, J. Chiles, J. Ma, and S. Fathpour, "Silicon-on-nitride waveguides for mid-and near-infrared integrated photonics," *Appl. Phys. Lett.* **102**(12), 121104 (2013).
37. K. McGarvey-Lechable and P. Bianucci, "Maximizing slow-light enhancement in one-dimensional photonic crystal ring resonators" *Opt.*, *Opt. Express* **22**(21), 26032–26041 (2014).
38. G. Xu, J. Wang, Q. Ji, M. Yang, T. Huang, J. Pan, Y. Xie, and P. Shum, "Design and analysis of slow-light Bloch slot waveguides for on-chip gas sensing," *J. Opt. Soc. Am. B* **37**(2), 257–263 (2020).